Volume 12 Number 3
2018
doi: 10.25923/xy6e-xt67

GSICS Quarterly

Editor: Manik Bali, ESSIC UMD

Newsletter–Fall 2018 Issue

CMA • CNES • EUMETSAT • IMD • ISRO • JAXA • JMA • KMA • NASA • NIST • NOAA • ROSCOSMOS . ROSHYDROMET • USGS • WMO

In This Issue

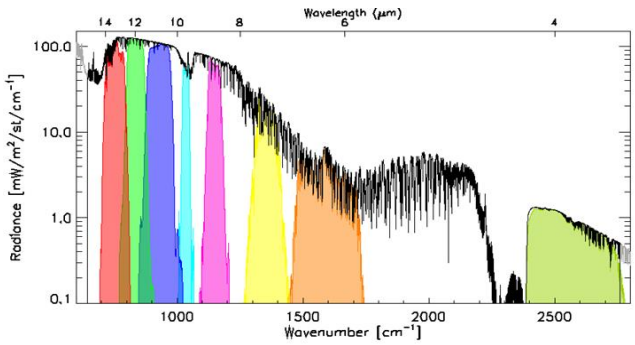

IASI-C spectra (above) overlaps with the Spectral Response Functions of SEVIRI channels 3-11 from right to left (coloured shaded areas) thereby providing unique opportunity conduct GSICS-style monitoring. (Curtesy: Hewison et al)

The image above shows the launch of MetOp-C on a Soyuz rocket

MetOp-C Successfully launched by Soyuz rocket on 7 November 2018

By Kenneth Holmlund, EUMETSAT and GSICS EP Vice Chair

On 7 November 2018, the Soyuz rocket placed the European weather satellite Metop-C in orbit. It is flying in the same-orbital plane as its predecessors Metop-A and –B, with the same instrument complement except for the HIRS, which Metop-C does not carry.

From a GSICS standpoint, this launch is significant because MetOp-C is also carrying the GSICS IR reference, the Infrared Atmospheric Sounding Interferometer (IASI). Similarly to IASI-A and IASI-B the new IASI would allow GSICS-style monitoring of Infrared instruments worldwide, providing continuity of the IASI measurements until mid-2020's and beyond. Currently IASI is the most commonly used instrument for monitoring GEO instruments by GSICS members and the new IASI onboard MetOp-C would provide continuity to reference scale measurements.

During the course of commissioning, the three Metops will fly in a so-called "tristar" configuration. Based on early user feedback, the decision will be made to either remain in a tristar phasing configuration or to shift Metop-C 180 degrees opposite Metop-B (original A/B configuration) with Metop-A in-between ("trident" configuration – see Figure 1, on the next page).

For most of its mission life, the Metop-C is expected to provide the primary service, with Metop-B located ~180° apart, providing a resilient observing capability. Based on the experiences with Metop-A and –B, it has been shown that two satellites in the same orbit provide higher impact on global Numerical Weather Prediction than a single satellite. The MetOp-B and MetOp-C (morning/evening) combination complements the

doi: 10.25923/xy6e-xt67

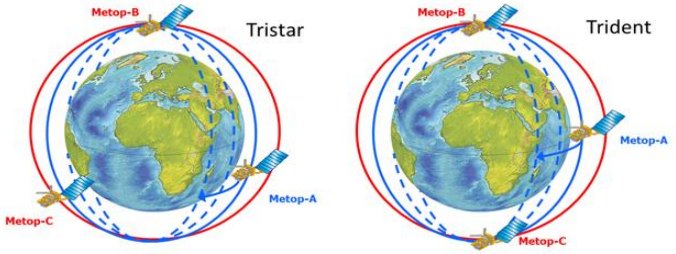

Figure 1: Left: Three MetOp's phasing with 120° separation (Tristar) adopted for SIOV and commissioning phase. Right: Trident phasing with 180° separation between MetOp-B and C and MetOp-A phased ~90° in-between.

Afternoon/Midnight observations of CrIS instruments onboard the JPSS mission. Since CrIS as well as IASI both are GSICS references the complete system will provide opportunities to monitor GSICS instruments at various times of the day. Additional details about the MetOp-C mission and data download links can be obtained from

https://www.eumetsat.int/website/home/TechnicalBulletins/Metop/DAT_4128787.html

Discuss the Article

GEO-LEO (Geostationary and Low-Earth-Orbit) Virtual-Dual-View Sensors: Towards Global Multi-GEO and Multi-LEO Consistency

by Yi Qin (CSIRO Oceans and Atmosphere) and Tim R. McVicar (CSIRO Land and Water), Canberra, Australia

Lack of sufficient measurements from single-view sensors has been a bottleneck in many remote sensing applications, limiting their potential utility. However, Hasekamp and Landgraf (2004) showed that multi-view data reduced the errors by an order of 2 when inverting aerosol parameters (size, optical depth and refractive indices) compared to single-view data. The current generation of geostationary satellites (Himawari-8/9, FY-4, GOES-R and MTG-I etc.), with increased temporal-spectral-spatial resolutions present a unique opportunity to overcome single-view sensor limitations. Here, we briefly review the method developed by Qin and McVicar (2018) to construct virtual-dual-view (VDV) remote sensing measurements by pairing compatible geostationary (GEO) and low-earth-orbiting (LEO) sensors, such that spectrally unified and radiometrically consistent observations from two view angles can be acquired with similar capacity as physical dual- / multi-view sensors such as AATSR and MISR.

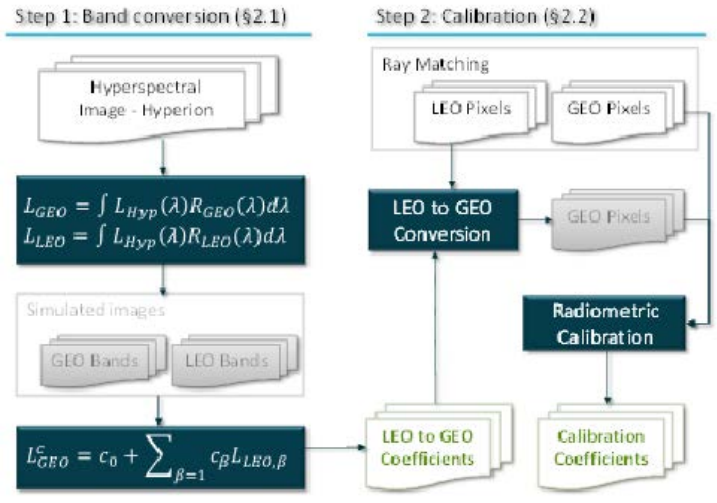

Figure 1: Flow chart showing the process implemented by Qin and McVicar (2018) to construct virtual-dual-view sensors from GEO-LEO sensors. White boxes represent the input images, and green texted boxes are the outputs of the process.

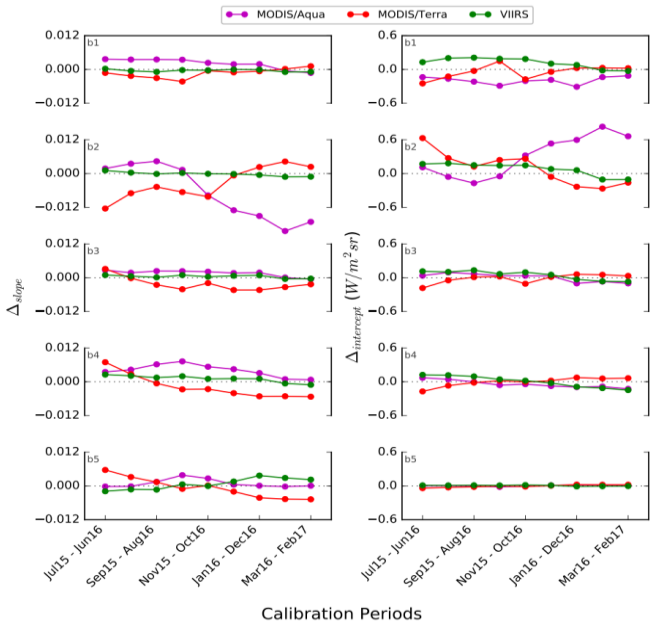

Figure 2: Temporal trend of the inter-calibration slope (left) and intercept (right) for the three sensor-pairs and AHI bands 1 to 5 (0.47, 0.51, 0.64, 0.86 and 1.61μm, from top to bottom, respectively.

doi: 10.25923/xy6e-xt67

Table 1. Radiometric inter-calibration results. Shown are the AHI band (center wavelength), number of valid matching points, slope, intercept and their standard error of, intercept p-value, the regression r-square, fitting error and bias. Units for the intercept, its standard error, and the fitting error and bias are in *W/m²sr*. Source: (Qin and McVicar 2018).

Band (CWL,μm)	N	Slope(b_b)		Intercept(a_b)			Regression		
		value	Std-err	Value	Std-err	p	r^2	Fit-err	Fit-bias
AHI–MODIS/Aqua									
0.47	2071	0.9701	0.0010	1.6810	0.2187	0.0000	0.9928	5.6907	0.0753
0.51	387	0.9376	0.0052	0.8404	0.3030	0.0055	0.9792	1.1248	0.1063
0.64	2079	1.0220	0.0011	1.0833	0.1597	0.0000	0.9928	5.0954	0.1592
0.86	1831	1.0328	0.0014	0.2842	0.1000	0.0045	0.9895	2.9091	0.1979
1.60	1750	1.0437	0.0020	0.2245	0.0213	0.0000	0.9852	0.4844	0.0288
AHI–MODIS/Terra									
0.47	2074	0.9421	0.0009	3.7255	0.1873	0.0000	0.9938	4.9675	-0.2338
0.51	667	0.9700	0.0036	-0.3080	0.2321	0.1846	0.9831	1.4156	0.0172
0.64	2081	1.0238	0.0009	1.0666	0.1260	0.0000	0.9941	4.1796	-0.1202
0.86	2033	1.0051	0.0010	0.7126	0.0811	0.0000	0.9933	2.6798	-0.0669
1.60	1855	1.0205	0.0017	0.3626	0.0185	0.0000	0.9882	0.4226	-0.0049
AHI–VIIRS									
0.47	757	1.0145	0.0009	2.0390	0.2340	0.0000	0.9974	4.2912	-0.0160
0.51	766	0.9718	0.0009	0.5203	0.2353	0.0270	0.9974	4.2117	-0.1146
0.64	1201	1.0305	0.0008	0.4704	0.1381	0.0007	0.9972	3.6981	-0.0235
0.86	1299	1.0142	0.0008	0.3519	0.0811	0.0000	0.9968	2.3058	-0.1036
1.60	2143	1.0390	0.0016	0.0299	0.0167	0.0732	0.9894	0.4148	0.0099

The procedure to construct VDV sensors is outlined in Figure 1 where the GEO sensor is AHI (Himawari 8) and the LEO sensors are MODIS (Aqua and Terra) and VIIRS respectively. First, the coefficients to convert LEO bands to GEO bands were derived from the simulated GEO-LEO simultaneous observations using multiple LEO bands in the proximity of each GEO band. For a wide-range of surface-types, the conversion error has been found to be small as shown in Table 1 and Figure 7 of Qin and McVicar (2018). In the second step, ray-matching was used to collect near-simultaneous observations from each of the GEO-LEO sensor pairs. Around the GEO's sub-satellite point, and for each LEO orbit, there is a point observed where the LEO and GEO satellites are linearly aligned providing a pair of surface measurements of the same point in the same view angle with essentially the same sun angle (i.e., ± 5 minutes). This very close match between GEO-LEO observations allows the use of both clear and cloudy pixels, providing a wide radiance range necessary for robust calibration. Finally, the matching LEO bands were converted to the corresponding GEO bands, and an inter calibration between the paired sensors was conducted. Table 1 shows the final results of the inter-calibration derived using data from Jul 2015 to Feb 2017 (20 months). It shows that the procedure is reliable and accurate as indicated by the high correlation, low error and negligible bias in the regression; these calibration coefficients are also comparable with previous studies (Tabata et al. 2016; Yu and Wu 2016). In addition to the unified GEO-LEO sensor pairs providing dual-view observation, the approach also allows the tracking of relative temporal radiometric drift between the paired sensors. Figure 2 shows that all the sensors (i.e., AHI (Himawari 8/9), MODIS (Aqua and Terra) and VIIRS) are very stable, in agreement with previous studies (Doelling et al. 2015; Wang and Cao 2016; Wu et al. 2016) for each band and sensor pair, respectively. The change of slope is less than 1% for most cases, well within the 2% MODIS calibration uncertainty (Xiong et al. 2018). Large variation for the 0.51 μm AHI-MODIS bands is likely regression fluctuation due to the use of the ocean color bands (10 and 11) which have small radiance range resulting in about ¾ of the GEO-LEO matched observations being removed due to

saturation (Qin and McVicar 2018). The network of GEO sensors provide near-global and continuous observation of Earth thus enabling the monitoring of various weather and climate variables. Consistency among the GEO sensors is crucial, for example, in global energy budget estimation. However, radiometric consistency among the GEO sensors is still work-in-progress. The VDV construction procedure described above provides a pathway towards global multi-GEO consistency, by calibrating all the GEO sensors to a common LEO sensor. Further, by then combining multiple radiometrically-consistent GEO sensors, other LEO sensors can potentially be calibrated against the same (set of) reference LEO sensor(s), leading to globally consistent multi-GEO-multi-LEO databases of original bands (single-view) or unified bands (dual-view).

References

Doelling, D.R., Wu, A.S., Xiong, X.X., Scarino, B.R., Bhatt, R., Haney, C.O., Morstad, D., & Gopalan, A. (2015). The Radiometric Stability and Scaling of Collection 6 Terra-and Aqua-MODIS VIS, NIR, and SWIR Spectral Bands. *IEEE Transactions on Geoscience and Remote Sensing, 53* (8), 4520-4535 (doi:4510.1109/Tgrs.2015.2400928)

Hasekamp, O.P., & Landgraf, J. (2004). Satellite remote sensing of aerosols: Information content of different measurement types. In, *Remote Sensing of Clouds and the Atmosphere IX* (pp. 260-269, doi:210.1117/1112.566374)

Qin, Y., & McVicar, T.R. (2018). Spectral band unification and inter-calibration of Himawari AHI with MODIS and VIIRS: Constructing virtual dual-view remote sensors from geostationary and low-Earth-orbiting sensors. *Remote Sensing of Environment, 209*, 540-550 (doi:510.1016/j.rse.2018.1002.1063)

Tabata, T., Andou, A., Bessho, K., Date, K., Dojo, R., Hosaka, K., Mori, N., Murata, H., Nakayama, R., Okuyama, A., & Takahashi, M. (2016). Himawari-8/AHI latest performance of navigation and calibration. In, *Proc. SPIE 9881, Earth Observing Missions and Sensors: Development, Implementation, and Characterization IV, 98812J (May 2, 2016); doi:10.1117/12.2240200*

Wang, W.H., & Cao, C.Y. (2016). Monitoring the NOAA Operational VIIRS RSB and DNB Calibration Stability Using Monthly and Semi-Monthly Deep Convective Clouds Time Series. *Remote Sensing, 8* (1), 32 (doi:10.3390/rs8010032)

Wu, A.S., Xiong, X.X., Cao, C.Y., & Chiang, K.F. (2016). Assessment of SNPP VIIRS VIS/NIR Radiometric Calibration Stability Using Aqua MODIS and Invariant Surface Targets. *IEEE Transactions on Geoscience and Remote Sensing, 54* (5), 2918-2924 (doi:2910.1109/Tgrs.2015.2508379)

Xiong, X., Angal, A., Barnes, W.L., Chen, H., Chiang, V., Geng, X., Li, Y., Twedt, K., Wang, Z., Wilson, T., & Wu, A. (2018). Updates of Moderate Resolution Imaging Spectroradiometer on-orbit calibration uncertainty assessments. In (pp. 18, doi:org/10.1117/1111.JRS.1112.034001): SPIE

Yu, F.F., & Wu, X.Q. (2016). Radiometric Inter-Calibration between Himawari-8 AHI and S-NPP VIIRS for the Solar Reflective Bands. *Remote Sensing, 8* (3), 165 (doi:110.3390/rs8030165)

Discuss the Article

doi: 10.25923/xy6e-xt67

Inter-Calibration of HY-1B/COCTS Thermal Infrared Channels with MetOp-A/IASI

by Mingkun Liu (Ocean University of China, China; University of Reading, UK), Christopher J. Merchant (University of Reading, UK), Lei Guan (Ocean University of China, China; Qingdao National Laboratory for Marine Science and Technology, China) and Jonathan P. D. Mittaz (University of Reading, UK)

The Haiyang-1B (HY-1B) satellite, operated by the National Ocean Satellite Application Center (NSOAS) of the State Oceanic Administration (SOA) of China, was launched in April 2007. The Chinese Ocean Color and Temperature Scanner (COCTS) on board the HY-1B satellite has two thermal infrared channels (#9 and #10) centred near 11 μm and 12 μm, respectively, which are intended for sea surface temperature (SST) observations, with a spatial resolution of 1.1 km at nadir (Pan et al., 2004). COCTS is a whiskbroom scanner, with four parallel detectors along-track. To improve the accuracy of COCTS SSTs, inter-calibration of COCTS thermal infrared radiance is carried out. The Infrared Atmospheric Sounding Interferometer (IASI) on board MetOp-A satellite is used as inter-calibration reference owing to its hyperspectral nature and high-quality measurements (Hewison et al., 2013).

The inter-calibration of HY-1B COCTS thermal infrared radiances with IASI is undertaken for data from the period 2009–2011 located in the northwest Pacific. Collocations of COCTS radiance with IASI are identified within a temporal window of 30 min, a spatial window of 0.12°×0.12° and an atmospheric path tolerance of 3%. Matched IASI spectra are convolved with the COCTS spectral response functions, while COCTS pixels within the footprint of each IASI pixel are spatially averaged, thus creating matched IASI-COCTS radiance pairs that should agree well in the absence of satellite biases. Because the spatial resolution of IASI is much larger than COCTS, the homogeneity of each IASI IFOV is very important. Radiance nonuniformity within the IASI IFOV increases the spatial uncertainties of matchups because of the different point spread functions between IASI and COCTS as well as increasing the uncertainty due to geolocation errors (Mittaz et al., 2011). We used the relative standard deviation, which is the (standard deviation)/mean of the COCTS valid pixels inside each IASI IFOV, to quantify the homogeneity. We also used a perimeter region outside the central collocation area to reduce the likelihood of time variable components such as errors caused by differences in the cloud and/or clear distributions in a similar way to that suggested by GSICS (Wu et al., 2009).

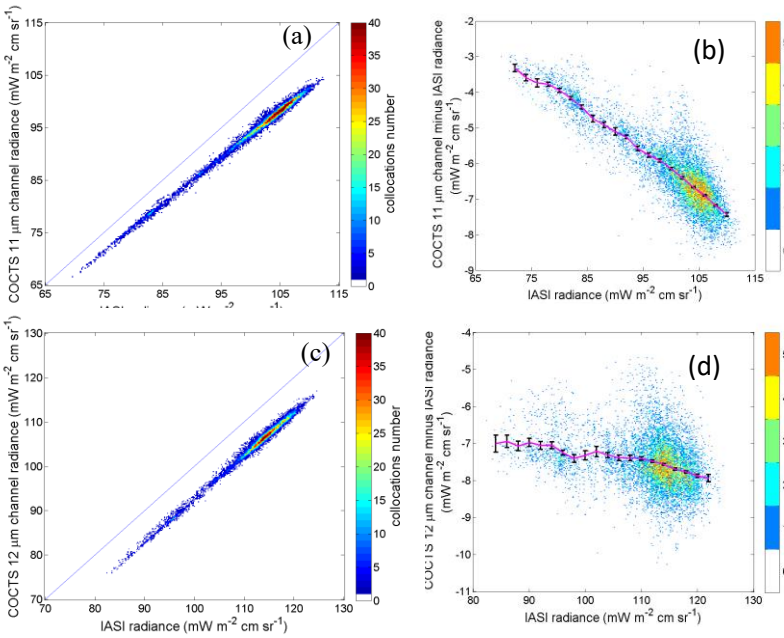

Figure 1. The scatter plots of COCTS: **(a)** 11 μm channel; and **(c)** 12 μm channel original radiance with IASI; and the variations of COCTS: **(b)** 11 μm channel; and **(d)** 12 μm channel original radiance minus IASI radiance difference

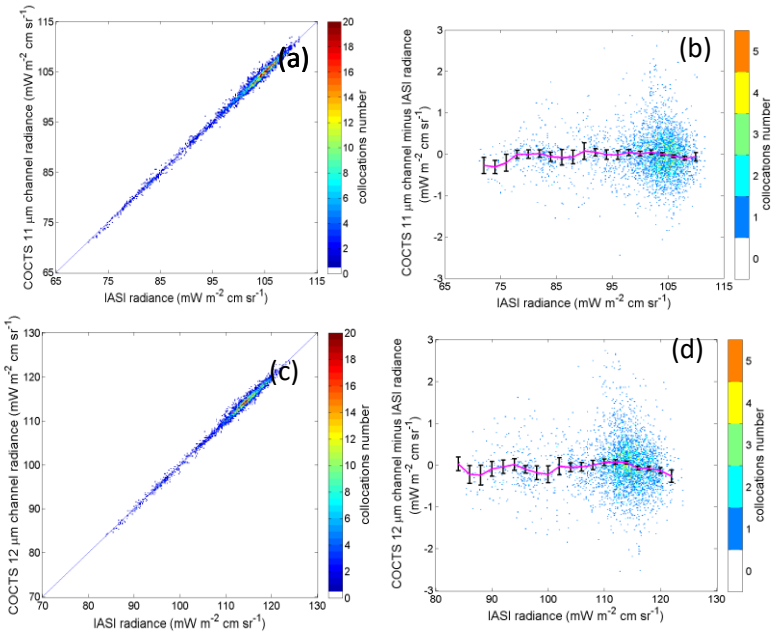

Figure 2. The scatter plots of COCTS: **(a)** 11 μm channel; and **(c)** 12 μm channel corrected radiance with IASI; and the variations of COCTS: **(b)** 11 μm channel; and **(d)** 12 μm channel corrected radiance minus IASI radiance difference against IASI radiance.

doi: 10.25923/xy6e-xt67

Table 1. The statistics of radiance and BT difference between COCTS and IASI before and after correction

	11 μm Channel Radiance Difference (mW m^{-2} cm sr^{-1})	11 μm Channel BT Difference (K)	12 μm Channel Radiance Difference (mW m^{-2} cm sr^{-1})	12 μm Channel BT Difference(K)
	Mean/Std.Dev	Mean/Std.Dev	Mean/Std.Dev	Mean/Std.Dev
Before correction	−6.37/0.95	−4.08/0.50	−7.57/0.62	−4.76/0.39
After correction	−0.02/0.51	−0.01/0.33	–0.01/0.57	–0.01/0.35

Based on these 11,250 filtered matchups, COCTS radiance from the 11 and 12 μm channels are compared with IASI. Figure 1(a) and (c) shows the scatter plots of COCTS 11 and 12 μm channel radiances with IASI radiances, respectively. The radiances of COCTS 11 and 12 μm channel are lower than IASI's with relatively large biases. The overall statistics of COCTS with IASI radiance indicate large cold biases of −6.35 mW m^{-2} cm sr^{-1} and −7.56 mW m^{-2} cm sr^{-1}, with the corresponding standard deviations of 0.96 mW m^{-2} cm sr^{-1} and 0.63 mW m^{-2} cm sr^{-1}. Figure 1 (b) and (d) indicates the variations of COCTS 11 and 12 μm channel radiance minus IASI radiance against IASI radiance, respectively. For COCTS 11 and 12 μm channel, both radiance differences represent approximately linear dependence on radiance. The difference for the COCTS 11 μm channel more obviously depends on scene radiance than for the 12 μm channel. In addition, the overall calibration of COCTS thermal infrared channels was stable from 2009 to 2011, except for the calibration drift at the beginning of April 2011.

The coefficients of COCTS radiance correction are obtained based on the filtered matchups of COCTS with IASI radiance. We use the robust linear regression to obtain the slope, a, and offset, b, of the relationship between COCTS minus IASI radiance difference and IASI radiance, represented as the Equation (1):

$$L_{COCTS} - L_{IASI} = a \times L_{IASI} + b \quad (1)$$

$$L'_{COCTS} = \frac{L_{COCTS} - b}{a + 1} \quad (2)$$

where the L_{COCTS} and L_{IASI} represent the COCTS and IASI original radiances, respectively. Because all the collocated radiance pixels of COCTS with IASI are larger than 65 m^{-2} cm sr^{-1} and 80 m^{-2} cm sr^{-1} for 11 and 12 μm channel respectively, the regression does not pass through zero. The COCTS original radiances are fitted to IASI data using Equation (1), therefore the COCTS corrected radiance L'_{COCTS} (substituting L'_{COCTS} for L_{IASI}) are given using Equation (2). A randomly selected subset, 2/3 of the whole matchup dataset, was used for regression and the remaining 1/3 were used for validation. Due to the calibration drifting at the junction point between March and April 2011, two periods during 2009 to 2011 are analysed separately for COCTS radiance correction. Period 1 is from January 2009 to March 2011 and the other period 2 is from April 2011 to December 2011. Coefficients for COCTS radiance corrections are calculated separately in period 1 and period 2. In addition, considering the different comparison results for COCTS four detectors, the regression coefficients for different COCTS detectors were obtained separately. The comparison results of COCTS 11 and 12 μm channel corrected radiance with IASI are shown as Figure 2. Figure 2 (a) and (c) shows scatter plots, while Figure 2 (b) and (d) presents the variations of radiance difference against IASI radiance after correction. Table 1 is the statistics of comparison results before and after correction based on the validation matchups. The large residual biases between COCTS original radiance and IASI radiance are removed after correction, with the value of −0.02 mW m^{-2} cm sr^{-1} and −0.01 mW m^{-2} cm sr^{-1} for 11 and 12 μm channels, respectively. For the 11 μm channel, the significant radiance-dependent pattern of radiance difference is corrected, with the reduced overall standard deviation from 0.95 mW m^{-2} cm sr^{-1} to 0.51 mW m^{-2} cm sr^{-1}. A reduction in the bias and standard deviation between the COCTS and IASI is also seen for the 12 μm channel. We have also provided the same statistics in brightness temperature (BT) space for ease of comprehension. As shown in Table 1, the overall mean differences of COCTS 11 and 12 μm channel original BTs with IASI are −4.08 K and −4.76 K, with the corresponding standard deviations of 0.50 K and 0.39 K. After correction, both mean values of COCTS 11 and 12 μm channel corrected BTs minus IASI are −0.01 K, with the corresponding standard deviations of 0.33 K and 0.35 K respectively. In addition, the significant striped noise of COCTS original radiance is reduced, which is evident in imagery and distributions of local standard deviation.

In conclusion, several strands of evidence indicate the calibration accuracy of COCTS is improved after the correction. In a future study, the COCTS corrected radiance will be applied to SST retrieval in the expectation that this will improve the COCTS SST accuracy.

Reference:

Pan, D., 2004, Future-generation satellites of Chinese ocean remote sensing. Sens. Syst. Next-Gener. Satell. VIII., Vol. 5570, 228–233, doi:10.1117/12.563894.

Hewison, T.J., Wu, X., Yu, F., Tahara, Y., Hu, X., Kim, D., Koenig, M., 2013, GSICS inter-calibration of infrared channels of geostationary imagers using Metop/IASI. IEEE Trans. Geosci. Remote Sens., Vol. 51, No. 3, 1160–1170, doi:10.1109/TGRS.2013.2238544.

Mittaz, J.; Harris, A., 2011, A physical method for the calibration of the AVHRR/3 thermal IR channels. Part II: An in-orbit comparison of the AVHRR longwave thermal IR channels on board MetOp-A with IASI. J. Atmos Ocean. Technol., Vol.28, No. 9, 1072–1087, doi:10.1175/2011JTECHA1517.1.

Wu, X.; Hewison, T.; Tahara, Y., 2009, GSICS GEO-LEO intercalibration: Baseline algorithm and early results. Atmos. Environ. Remote Sens. Data Process. Util. V: Read. GEOSS III 2009, 7456, doi:10.1117/12.825460.

Discuss the Article

Coming Soon: OCO-3

by Robert Rosenberg, Gary Spiers, Richard Lee, Shanshan Yu, David Crisp, Annmarie Eldering (Jet Propulsion Laboratory, California Institute of Technology) and Stephen Maxwell (National Institute of Standards and Technology)

The Orbiting Carbon Observatory-3 (OCO-3) is NASA's second instrument dedicated to monitoring carbon dioxide from space. Following installation on the International Space Station (ISS) in early 2019, it will continue the record of space-based measurements through 2022. It will join Japan's Greenhouse gases Observing Satellites, GOSAT and GOSAT-2 which launched in 2009 and 2018, respectively, and NASA's OCO-2, which was launched in 2014.

The core OCO-3 instrument is the inherited spare from OCO-2, with three high-resolution imaging grating spectrometers that share a common entrance telescope. One channel measures the molecular oxygen A-band from 758 nm to 773 nm, and the others measure "weak" and "strong" carbon dioxide bands spanning 1591 nm to 1623 nm and 2042 nm to 2083 nm. The oxygen spectrometer also observes the Fraunhofer lines, enabling retrievals of Solar Induced chlorophyll Fluorescence (SIF). Each channel uses 1016 detector pixels in the spectral dimension and averages 160 detector pixels in the spatial dimension into 8 footprints. Science data is acquired at three frames per second, and there is an additional calibration mode where 220 spatial rows are returned at a greatly reduced frame rate.

The payload of OCO-3 has substantial differences from the OCO-2 satellite. The most substantial of these is the pointing capability. While OCO-2 spins the spacecraft to point the instrument, OCO-3 will be installed on the ISS' Japanese Experiment Module - Exposed Facility (JEM-EF) and will use a two-axis Pointing Mirror Assembly (PMA) to provide pointing capability. The on-board calibration system is also different: OCO-2 uses a diffusive reflective panel built into the instrument body that moves in/out of the telescope field of view to provide illumination from the calibration lamps while OCO-3 uses the PMA to point to a separate lamp calibration assembly. The PMA also offers the ability to acquire target observations more frequently, and has a new area mapping mode to scan 100 km x 100 km regions of interest. To maintain footprint sizes equivalent to OCO-2, OCO-3 has a new telescope that provides a wider field of view to compensate for the lower altitude of the ISS providing each of the eight spatial footprints with an area slightly less than 3 square kilometers. OCO-3 also carries a pair of context cameras to aid with geolocation.

Utilizing the ISS platform adds many new opportunities and also presents new challenges. Complementary measurements from other instruments such as ECOSTRESS and GEDI will allow scientists to understand ecosystem processes using CO_2, evapotranspiration, and biomass data. The precessing orbit will yield more data at mid- latitudes, but on the other hand will never measure extreme latitudes. The ability to observe reflected sunlight at varying times of day is also a significant contrast to OCO-2, which as part of the sun-synchronous "A-Train" constellation always observes at 13:30 local time.

The preflight calibration of OCO-3 followed the same approach as for OCO-2. Thermal vacuum tests in 2013,

doi: 10.25923/xy6e-xt67

2016, and 2017 were performed at different stages of instrument development, and the final thermal vacuum test of the integrated payload was completed in July 2018. Radiometric calibration was performed using an external integrating sphere that was characterized in situ by NIST. Two spectro-radiometers repeatedly viewed NIST standard sources, then viewed the JPL source through the chamber window prior to Payload testing. OCO-3's enlarged field of view presented a new challenge because the sphere was less uniform over a larger area. Spectral calibration was again performed with tunable laser sources, with improved data density at the band edges. Other calibrations measured spatial field of regard, focus, alignment of the spectrometer slits, alignment of internal polarizers, calibration lamp intensity, noise, masking of outlier detector pixels, and dark current. Finally, a critical validation was provided by simultaneous uplooking direct-sun measurements by OCO-3 and a Fourier Transform Spectrometer from the Total Column Carbon Observing Network (TCCON) in April 2018. Applying the radiometric and spectral calibration coefficients to solar data with atmospheric absorption is a crucial test for all of the processes described above.

The inflight calibration of OCO-3 will use a very limited dataset compared to the preflight characterization. Spectral calibration cannot be measured, though the performance of the retrieval algorithms does yield some insight into how it changes over time. Radiometric degradation is measured using the on-board lamps, but distinguishing changes in the calibrator from changes in the instrument has proven difficult on OCO-2 and will be more difficult on OCO-3. OCO-2 has a solar diffuser and is able to observe the moon twice each month, while OCO-3 can never view the sun and will have less frequent and lower quality lunar measurements. Therefore, vicarious calibrations at Railroad Valley, NV, observations of pseudo-invariant desert sites in the Sahara, Arabian, and Namib deserts, and cross-calibration with other satellites will play a more critical role. There is one notable aspect of calibration that is of higher quality during flight than in ground testing: the sensitivity of dark signal to temperature is characterized much better because it is measured over a dozen times each day.

Like OCO-2, the science goal of OCO-3 is to collect the measurements needed to quantify natural and anthropogenic CO_2 sources and sinks on regional scales and track their changes over monthly to interannual time scales. This requires "full physics" retrievals of total column carbon dioxide to have precision better than 1 ppm, which is less than 0.25%. The seasonal patterns and year-to-year differences in the carbon cycle also require instrument performance to be stable, with any changes with time carefully characterized. Following two months of in-orbit checkout activities, OCO-3 will begin taking over 100,000 measurements each day, out of which tens of thousands of soundings will pass cloud screening and other filters.

Figure above shows the OCO-3 payload being inserted into the thermal vacuum chamber for testing in the 'feet up' position. The interface for the Japanese Exposed Facility on the International Space Station is on the left end of the payload, and the fixtures used to attach the payload to the Dragon Capsule are facing upwards in the picture. The payload is loaded in this orientation so light can be introduced through a window at the top of the thermal vacuum chamber.

The team expects to start delivering calibrated, geolocated spectral radiances to the NASA Goddard Earth Sciences Data and Information Services Center (GES DISC) in late 2019. The mission will continue into 2022.

The research was carried out at the Jet Propulsion Laboratory, California Institute of Technology, under a contract with the National Aeronautics and Space Administration.

Discuss the Article

doi: 10.25923/xy6e-xt67

NEWS IN THIS QUARTER

EUMETSAT METEOROLOGICAL SATELLITE CONFERENCE 2018

Highlights of 2018 EUMETSAT Meteorological Satellite Conference

by Tim Hewison, EUMETSAT

About 400 users of EUMETSAT satellite data took part in the week-long conference from 17-21 September 2018 which coincided with Estonia's 100th anniversary celebrations.

The conference focused on the requirements and challenges for satellite weather and climate monitoring in high latitudes. This included plenary sessions on future requirements for data supporting aviation services, particularly related to the specific challenges of routing over or near the North Pole and weather forecasting for Baltic or Nordic areas. But also high on the agenda were preparations for the next generations of EUMETSAT satellites.

From a GSICS perspective, highlights included:

- Dave Doelling (NASA) reported good progress in the application of Deep Convective Cloud and Pseudo Invariant Calibration Sites to Shortwave Infrared channels.
- Tasuku Tabata (JMA) presented a dataset of re-calibrated Infrared and Water Vapor channels' measurements from JMA and EUMETSAT geostationary satellites, which exploited the *Prime GSICS Correction* concept to combine multiple reference instruments.
- Hanlie Xu (CMA) described the inter-calibration of MERSI and HIRAS on FY-3D.
- Eun-kyu Kim (KMA) presented a long term analysis of COMS visible channel calibration using vicarious method and Moon observations.
- Tim Hewison (EUMETSAT) presented an analysis of the impact of GSICS Corrections on Meteosat/SEVIRI Level-2 Products, which showed a small improvements - comparable to the magnitude of errors introduced by not accounting for Meteosat-8's high inclination orbit.
- Xiaoxiong Xiong (NASA) and Dave Tobin (SSEC) reviewed the performance of the VIIRS and CrIS instruments on NOAA-20, respectively.
- Several presentations showed interesting results from the FIDUCEO project, including Frank Rüthrich (EUMETSAT), who presented an FCDR from more than 35 years of Meteosat First Generation visible band observations, and Ralf Giering (FastOpt), who presented a novel framework to harmonise AVHRR and ATSR data series for climate applications.
- There was also a strong presence in the microwave domain, including Timo Hanschmann (EUMETSAT), investigating the inter-instrument bias of current microwave humidity sounders, Ed Kim (NASA) describing possible SI-Traceable calibration of satellite microwave radiometers and Ralf Bennartz, who introduced TROPICS - cubesat constellation of microwave imagers, which will rely on operational inter-calibration.

The presentations will be available on the EUMETSAT conference website: https://www.eumetsat.int/website/home/News/ConferencesandEvents/DAT_3647214.html

Discuss the Article

doi: 10.25923/xy6e-xt67

Microwave inter-calibration activities reported at MicroRad 2018

by Vinia Mattioli, EUMETSAT

The 15th Specialist Meeting on Microwave Radiometry and Remote Sensing of the Environment (MicroRad 2018) took place this year in Cambridge, MA, USA, on March 27-30, hosted by the Massachusetts Institute of Technology. Microrad is a unique gathering where the microwave radiometry community has the opportunity to present current and future microwave missions, instrument designs, research results and applications in the field of microwave remote sensing, to an audience that comprises academia, industry and meteorological operational agencies. The Golden Florin (Fiorino Oro) Award is presented at the conference to individuals who throughout their career have made outstanding contributions to research in Passive Microwave Remote Sensing. The award was established in 1995 by the Center for Microwave Remote Sensing (CeTeM, Italy) now sponsored jointly with the IEEE Geoscience and Remote Sensing Society (GRSS). The recipient in 2018 was Philip W. Rosenkranz, Massachusetts Institute of Technology (retired) in recognition of his work on theoretical models and measurements for absorption by molecular oxygen, water vapor, and cloud liquid water with microwave radiometers.

The technical program of MicroRad'18 included three presentations specifically devoted to microwave inter-calibration, in the framework of the NASA's Precipitation Measurement Missions (PMM) Intercalibration Working Group (XCal).

Wesley Berg (Colorado State University) provided a wide overview of the approaches used to intercalibrate radiometers in the Global Precipitation Mission (GPM) and Tropical Rainfall Measuring Mission (TRMM) constellations [1]. Several of the calibration corrections that have been developed by XCAL and associated lessons learned in terms of instrument design and on-orbit calibration characterization were addressed. Finally, considerations and challenges related to CubeSat/SmallSat missions were also discussed.

A specific presentation [2] was given by Rachel Kroodsma (Univ. of Maryland) to describe the expansion of the GPM constellation intercalibration data record, to include radiometers in operation since the launch of TRMM. More specifically, the Advanced Microwave Sounding Units (AMSU-B), on-board the NOAA-15, NOAA-16, and NOAA-17 platforms were NOAA-15 and NOAA-16 both showed analyzed and inter-calibration constants delivered. AMSU-B instruments on significant time-dependent and scan-dependent calibration issues while NOAA-17 showed relative stability similar to the higher-quality Microwave Humidity Sounder (MHS) instruments on the NOAA-18, NOAA-19, Metop-A, and Metop-B platforms.

Finally, an uncertainty estimation model, developed for the radiometric intercalibration between GPM Microwave Imager (GMI) and a given constellation radiometer was described in a poster presentation by Ruiyao Chen and W. Linwood Jones (Univ. of Central Florida) [3]. With this method, an uncertainty is associated to each source of the bias computed with XCal double difference (DD) technique. The presented results showed the analysis with respect to TRMM Microwave Imager (TMI).

References

[1]https://www2.securecms.com/MicroRad2018/Papers/viewpapers.asp?papernum=1061

[2]https://www2.securecms.com/MicroRad2018/Papers/viewpapers.asp?papernum=1098

[3]https://www2.securecms.com/MicroRad2018/Papers/viewpapers.asp?papernum=1099

Discuss the Article

Participants in the 15th Specialist MicroRad 2018

doi: 10.25923/xy6e-xt67

Announcements

The Characterization and Radiometric Calibration for Remote Sensing (CALCON) Annual Meeting will be held June 17–20, 2019 at the Space Dynamics Laboratory in Logan, UT

by James J. Butler, Xiaoxiong (Jack) Xiong ,(NASA), Deron Scott and Stephanie Halton (SDL)

Now in its 28th year, the Characterization and Radiometric Calibration for Remote Sensing (CALCON) Annual Meeting provides a forum for scientists, engineers, and managers to present, discuss, and learn about calibration, characterization, and radiometric issues within the microwave, IR, visible, and UV spectral ranges. Individuals developing measurement requirements for current and future sensor systems are encouraged to participate in the meetings to foster continuity and advancement within the community. CALCON attendance promotes interaction with other experts and helps close the gap between expectations and real-world experiences. Collaboration often results in the discovery of solutions to individual program challenges.

Meeting information and abstract submittal is available at www.calcon.sdl.usu.edu. February 1, 2019 is the deadline for the Call for Papers.

Call for SPIE Optics and Photonics Earth Observing Systems XXIV conference to be held in San Diego Aug 11-15, 2019

by James J. Butler and Xiaoxiong (Jack) Xiong, NASA

The annual SPIE Optics and Photonics' Earth Observing Systems XXIV Conference will be held August 11-15, 2019 at the San Diego Convention Center, San Diego, CA.

SPIE. The international society for optics and photonics

The Earth Observing Systems XXIV conference welcomes the submission of papers over a wide range of remote sensing topics. Papers are solicited in the following general areas:

- Earth-observing mission studies including new system requirements and plans
- Commercial system designs
- Electro-optical sensor designs and sensitivity studies
- Ultraviolet through thermal infrared, microwave, radar, and lidar remote sensing systems
- Hyperspectral remote sensing instruments and methodologies
- Instrument sub-system and system level pre-launch and on-orbit calibration and characterization
- Vicarious calibration techniques and results
- Satellite instrument airborne simulators
- Techniques for enhancing data processing, reprocessing, archival, dissemination, and utilization
- Conversion from research to operational systems
- On-orbit instrument inter-comparison techniques and results
- Enabling technologies (optics, antennas, electronics, calibration techniques, detectors, and models)

- Sensor calibration traceability, uncertainty, and pre-launch to on-orbit performance assessments
- Lunar radiometry and photometry
- Remote sensing data acquisition and analysis.

The conference call for papers is available online at https://spie.org/OPO/conferencedetails/earth-observing-systems?SSO=1 . Conference abstracts are due January 30, 2019, and proceedings manuscripts are due July 17, 2019

GSICS-Related Publications

Calbet, X., Peinado-Galan, N., DeSouza-Machado, S., Kursinski, E. R., Oria, P., Ward, D., Otarola, A., Rípodas, P., and Kivi, R.: Can turbulence within the field of view cause significant biases in radiative transfer modeling at the 183 GHz band?, Atmos. Meas. Tech., 11, 6409-6417,doi: 10.5194/amt-11-6409-2018, 2018.

Coldewey-Egbers, M., Slijkhuis, S., Aberle, B., Loyola, D., and Dehn, A.: The Global Ozone Monitoring Experiment: review of in-flight performance and new reprocessed 1995–2011 level 1 product, Atmos. Meas. Tech., 11, 5237-5259,doi: 10.5194/amt-11-5237-2018, 2018.

J. X. Yang and H. Yang, "Radiometry Calibration With High-Resolution Profiles of GPM: Application to ATMS 183-GHz Water Vapor Channels and Comparison Against Reanalysis Profiles," in *IEEE Transactions on Geoscience and Remote Sensing*. doi: 10.1109/TGRS.2018.2861678.

N. Xu *et al*., "Prelaunch Calibration and Radiometric Performance of the Advanced MERSI II on FengYun-3D," in *IEEE Transactions on Geoscience and Remote Sensing*, vol. 56, no. 8, pp. 4866-4875, Aug. 2018. doi: 10.1109/TGRS.2018.2841827

Toté, C.; Swinnen, E.; Sterckx, S.; Adriaensen, S.; Benhadj, I.; Iordache, M.-D.; Bertels, L.; Kirches, G.; Stelzer, K.; Dierckx, W.; Van den Heuvel, L.; Clarijs, D.; Niro, F. Evaluation of PROBA-V Collection 1: Refined Radiometry, Geometry, and Cloud Screening. *Remote Sens.* **2018**, *10*, 1375.doi: 10.3390/rs10091375

Submitting Articles to GSICS Quarterly Newsletter:

The GSICS Quarterly Press Crew is looking for short articles (800 to 900 words with one or two key, simple illustrations), especially related to calibration / validation capabilities and how they have been used to positively impact weather and climate products. Unsolicited articles may be submitted for consideration anytime, and if accepted, will be published in the next available newsletter issue after approval/editing. Please send articles to manik.bali@noaa.gov.

With Help from our friends:

The GSICS Quarterly Editor would like to thank Tim Hewison (EUMETSAT), Sri Harsha Madhavan (SSAI) and Lawrence E. Flynn (NOAA) for reviewing articles in this issue.

Published By

GSICS Coordination Center
NOAA/NESDIS/STAR NOAA
Center for Weather and Climate Prediction,
5830 University Research Court
College Park, MD 20740, USA